Detection of Multipath Propagation Effects in SAR-Tomography with MIMO Modes

Tobias Rommel, German Aerospace Centre (DLR), tobias.rommel@dlr.de, Germany
Gerhard Krieger, German Aerospace Centre (DLR), gerhard.krieger@dlr.de, Germany

Abstract

This paper introduces a Multiple-Input Multiple-Output (MIMO) concept for Synthetic Aperture Radar (SAR) tomography. Basic idea is to localize multipath propagation effects with a combined transmit and receive Digital Beam Forming (DBF) technique. Major part of this paper is attended to the description of a MIMO-radar experiment, conducted for a final proof of concept. For this experiment, a ground-based MIMO-radar was placed on top of a building, while the antenna array was looking downwards to a dihedral scatterer placed on a meadow. In addition, the equivalent phase center of the target was covered with absorbing material to avoid direct reflections. By using an antenna beam configuration, where the transmit and the receive antenna beams are looking to the equivalent phase center of the dihedral scatterer, it was possible to suppress the target. In a repeated processing of the same acquired data set, where each of the antenna beams illuminates one of the two perpendicularly aligned surfaces of the dihedral scatterer, the target appeared in the range compressed data.

1 Introduction

In standard SAR, the range and azimuth signals are mapped into a 2-dimensional image, while information about the target height is not available. To extract also height information about the target scene, in repeat-pass and single-pass SAR tomography multiple receive antennas orientated along elevation are used to estimate the Angle of Arrival (AoA) along that direction and to generate accordingly 3-dimensional maps [1], [2].

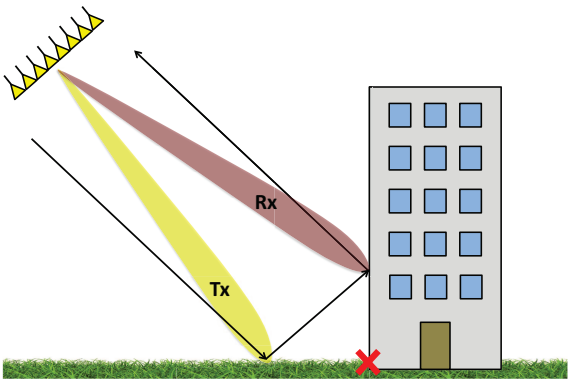

Figure 1: Principle of multipath detection with transmit and receive beams pointing to different directions. The cross at the edge of the building indicates the equivalent phase center of the reflection.

With respect to [3], in presence of multipath scattering, the true target position can not be determined correctly via SAR tomography using a single-pass system with one transmitter and multiple receivers. The reason can be given with an example illustrated in Fig. 1. From dihedral scatttering it is known, that the effective phase center position is located at the intersection point of two perpendicular surfaces. This point is marked with a red 'x' in the figure and equal to the determined position of the multipath scattering mechanism measured via repeat-pass SAR tomography. In single-pass tomography, the receive beamformer always focuses to the position of the last scatterer and hence, the surface of the house and the ground are seen as individual targets. Obviously, both results are incorrect.

To overcome the described measurement error, in [3] it is suggested to use in addition to the multiple receive antennas also multiple transmit antennas, transmitting orthogonal waveforms. In case of redundant antenna phase centers, it is possible to form individual Tx-Rx antenna beam combinations in the post processing. After separation of the orthogonal waveforms, $N_{\mathrm{Tx}} \cdot N_{\mathrm{Rx}}$ raw data sets are available, where N_{Tx} and N_{Rx} are the numbers of transmit and receive antennas. Using a linear Digital Beam Forming (DBF) algorithm, individual phase weights for each Tx-Rx channel combination can be applied to form independent transmit and receive antenna beams by final signal summation. This can be followed by standard SAR processing, such as range and azimuth compression.

If it is assumed, that the transmit and the receive beams point at the same time to different directions, as indicated in Fig. 1, just dihedral scattered signals can be detected, while direct scattering mechanisms are suppressed. If both beams point to the same direction, it is vice versa and dihedral scatterers are suppressed, while direct scattering becomes visible. If the output of both steering methods is compared, it is possible to locate multipath propagation effects and to correct them. To proof this MIMO-SAR technique, a ground-based MIMO-radar measurement was conducted. The setup is described in the next section.

2 Experiment Description

Since the aforementioned concept has to be applied for each azimuth position of a SAR data set separately, for a first proof it is sufficient to conduct the experiment in the range / elevation direction for a single snapshot with a static MIMO-radar. This has the advantage, that no additional errors may be added. Basic aim of the experiment is to identify two perpendicularly aligned metal plates unambiguously as a dihedral scatterer. A gap around the virtual phase center at the edge of the metal plates should show that there is no reflection if the antenna beam is steered to that point. Details of the scene and the antenna array are given next.

2.1 Radar, Scene and Signals

A MIMO-radar system with four transmit and eight receive channels, operating in X-band at a center frequency of $f_0 = 9.58$ GHz was placed on top of the roof of a building (more information about the radar can be found in [4]). A sketch of the measurement setup is shown in Fig. 2. Three trihedral corner reflectors at ground range distances of 20.4 m, 24.4 m and 28.4 m served as reference point targets for later signal calibration.
Two metal plates of size 0.5 m x 1.0 m each, both placed at slant-range distances of approximately 18.8 m, are used as a double bounce target. The incident wave on the horizontally aligned plate is reflected forward to the vertical plate, which reflects the signal back to the radar and reciprocally. The angle of the phase center at the virtual intersection point was $\Theta_2 = 49.9°$. According to the chosen geometry, it is assumed that the plates can not be resolved as dihedral scatterer after standard range compression or standard tomographic processing, e.g. single-pass SAR tomography. Further it is expected, that no reflections occur at the absorbing material, on which the vertical metal plate is placed.
Sole objective of this experiment is the proof of the suggested MIMO concept. To avoid effects caused by not perfectly orthogonal waveforms and since the scene does not change over time, the transmit signals were transmitted in a time-multiplex mode, while all receive channels were acquired simultaneously. Finally, neglecting coupling effects, orthogonal data sets for each channel combination are available. As transmit waveforms served up-chirp signals with a pulse duration of 10 μs and 300 MHz bandwidth.

2.2 Antenna Array

Two antenna carriers mounted on a handrail at the roof edge of the building are used to fix the transmit and receive antennas (cf. Fig. 3). A horizontal separation between the transmit and receive antenna phase centers of 0.50 m avoided too high coupling effects. While the receive antennas were standard gain horn antennas with a gain of 10.0 dBi and Half-Power Beam Widths (HPBW's) along elevation of $\Delta\Theta_{3\text{dB,el}} = 48.5°$ and along azimuth of $\Delta\Theta_{3\text{dB,az}} = 47.4°$, for transmission patch antennas with a gain of 14.1 dBi and HPBW's of $\Delta\Theta_{3\text{dB,el}} = 60°$, $\Delta\Theta_{3\text{dB,az}} = 16°$ were used.

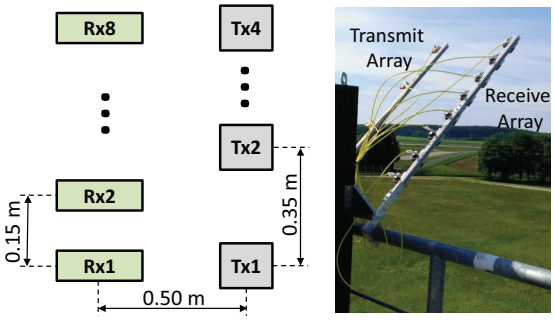

Figure 3: Sketch and photo of the antenna array used for the experiment.

The element spacing of the eight receive antennas was chosen to be $d_{\text{Rx}} = 0.15$ m, whereas the distance between the four transmit antennas was $d_{\text{Tx}} = 0.35$ m (compare Fig. 3). This leads to minimum HPBW's of the synthesized antenna beams of $\Delta\Theta_{\text{Rx,3dB}} = 1.1°$ for receive and $\Delta\Theta_{\text{Tx,3dB}} = 1.3°$ for transmit. Due to the large element spacings in comparison to the signal wavelength, grating lobes will appear along the elevation angle at $\Theta_{\text{GL,Tx}} \approx \arcsin\left(c_0/(f_0 \cdot d_{\text{Tx}})\right) = \pm 5.1°$ in the transmit case and at $\Theta_{\text{GL,Rx}} \approx \arcsin\left(c_0/(f_0 \cdot d_{\text{Rx}})\right) = \pm 12.0°$ in the receive case. In relation to the measurement scene, the chosen geometry of the antenna array enables to form two different antenna beam configurations, which can be used to proof the concept.

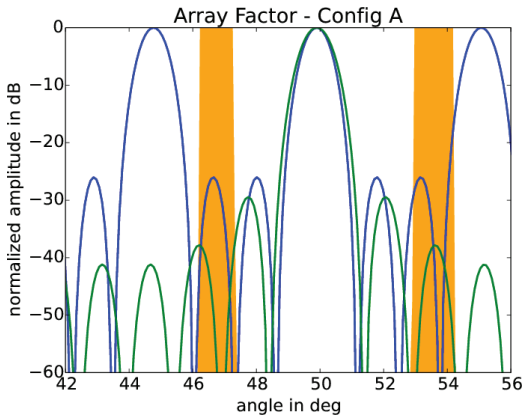

Figure 4: Array factor of the transmit (blue) and receive (green) antenna beams pointing to the same direction: $\Theta = 49.9°$.

In beam-configuration A, the transmit and the receive antennas are pointing to the same direction. An example is given in Fig. 4, where the array factors of the transmit (blue color) and receive (green color) antenna beams are plotted with a steering to $\Theta = 49.9°$. The orange colored areas indicate the positions of the two metal plates. It turns out that the combined Tx-Rx beam-steering in this configuration can image at maximum one of the two plates. Imaging both plates simultaneously would not be possible. In beam-configuration B, the antenna arrays

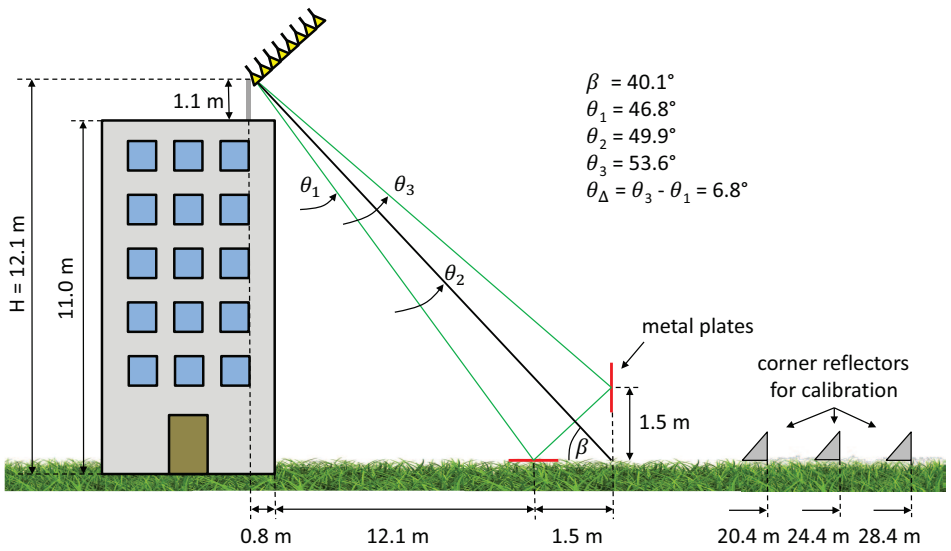

Figure 2: Sketch of the measurement setup used for the multipath propagation detection experiment.

point to different directions with an offset of $\Theta_\Delta = 6.8°$ (see Fig. 5). Using this value, at the same time, each metal plate is illuminated with another antenna beam. Hence, in this configuration, the plates should be visible. In the plots of the array factor we can also see, that the first grating lobe of the transmit antenna is set within the area of interest (due to the limited number of available transmit channels). However, this should not lead to any disturbances, because a null of the antenna beam falls into the main-lobe of the receive antenna. Finally, the Tx and Rx antennas are sufficiently encoupled.

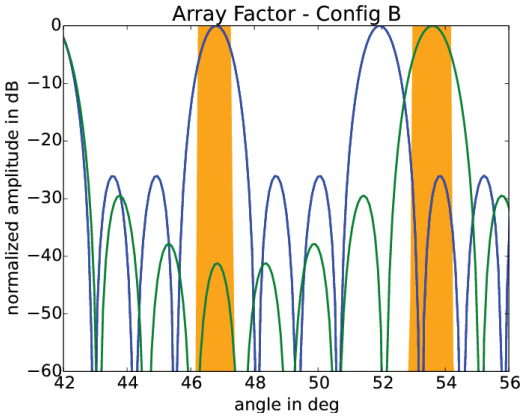

Figure 5: Array factor of the transmit (blue) and receive (green) antenna beams pointing to different directions: $\Theta = 46.8°$, $\Theta_\Delta = +6.8°$.

3 Calibration, Processing and Measurement Results

Beginning with the calibration concept, apart from the pre-processing and calibration steps used to synchronize the channels of the radar hardware, additional signal calibration is applied to increase the quality of the processed results. Especially due to the short ranges between radar and target and due to the large extent of the antenna array in comparison to the scene, a highly accurate synchronization between the channels becomes mandatory.

The first signal correction step is the compensation of the free-space attenuation according to the Friis equation. This leads to an amplification by the power of four along range direction. Next, the data set of each channel combination is individually range compressed leading to $N_{\mathrm{Tx}} \cdot N_{\mathrm{Rx}} = 4 \cdot 8 = 32$ range profiles of the observed scene. An example of the corrected and range compressed signal for the first channel combination (Tx1 & Rx1) can be found in Fig. 6. While the three trihedral corner reflectors appear with the same normalized amplitude of 0.0 dB, the metal plates with a lower radar cross section caused an amplitude of -13.6 dB. The ground range positions agree with those mentioned in Fig. 2.

According to the phase estimation method described in [5], the range compressed signal is divided into three range bins, while each bin contains the scattering response of a single corner reflector. Then, the phase course of each bin is computed and compared to the simulation, while redundancy due to multiple transmit channels helped to decrease the synchronization errors by calculation of the mean values. This leads to the last applied calibration step, where the mean values of the estimated phases of the measurement data were adapted to the phases from the model of the computer simulation.

Because of the large element spacing, each antenna has another looking angle for each target, which complicates the DBF processing. While in standard receive-only DBF algorithms only the far-field condition holds, we have to generalize this concept for the near-field. This leads to a multistatic formulation of the radar geometry. The expression for the signal delay from the transmit antenna with index k to the ground and back to the receive antenna with index i reads as follows:

$$\tau_{k,i}(t) = \frac{\|\boldsymbol{r}_{\mathrm{Tx},k}(t)\| + \|\boldsymbol{r}_{\mathrm{Rx},i}(t)\|}{c_0}, \qquad (1)$$

while t denotes the time, c_0 is the speed of light, $\|...\|$ denotes the Euclidean norm and $\boldsymbol{r}_{\mathrm{Tx},k}(t)$ and $\boldsymbol{r}_{\mathrm{Rx},i}(t)$ are the time-variant range vectors from the transmit antenna to the target position and back to the receive antenna. For near-field focusing, these time delays are calculated for each ground range position in dependency on t. Taking the antenna pair with indexes $k = i = 1$ as reference, next we define a differential time delay with the property

$$\Delta\tau_{k,i}(t) = \tau_{k,i}(t) - \tau_{1,1}(t). \qquad (2)$$

For beam forming it is necessary to shift each range compressed data set $s_{k,i}(t)$ by the delays $\Delta\tau_{k,i}(t)$:

$$u_{k,i}(t) = s_{k,i}\left(t - \Delta\tau_{k,i}(t)\right). \qquad (3)$$

Usually this is done in signal processing with the time-shifting property of the Fourier transform in frequency domain. A final summation of $u_{k,i}(t)$ over all channels leads to the range compressed and spatially filtered range profile of the illuminated scene:

$$u_{\mathrm{DBF}}(t) = \sum_{k=1}^{N_{\mathrm{Tx}}} \sum_{i=1}^{N_{\mathrm{Rx}}} u_{k,i}(t). \qquad (4)$$

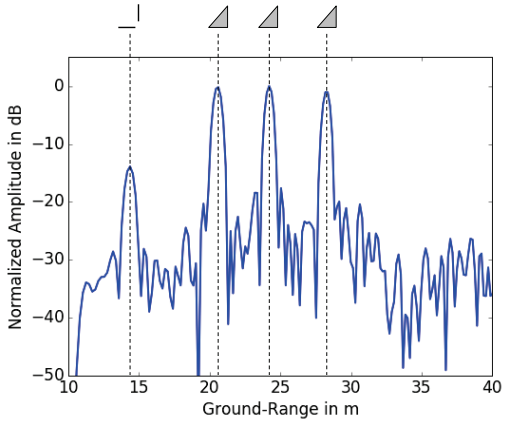

Figure 6: Exemplary range-compressed and calibrated data set of the first transmit and receive channel: $|s_{1,1}(t)|^2$.

In the following, we concentrate on the previously mentioned antenna beam configurations A and B.
In configuration A, the transmit and the receive beams point to the same direction ($\Theta_\Delta = 0°$). The weighted and combined range compressed data are depicted in Fig. 7. In comparison to the uncombined data from Fig. 6, the resulting DBF gain measured at the corner reflectors is 14.4 dB. The theoretical gain of $10 \cdot \log\{N_{\mathrm{Tx}} \cdot N_{\mathrm{Rx}}\} = 15.1$ dB could not be achieved due to remaining calibration errors (in particular the topography of the ground). As it becomes clearly visible, the metal plates appear suppressed with a maximum amplitude of just -22.3 dB. This stands strongly in agreement with the side-lobe level of the array factor (Fig. 4). In fact, in comparison to Fig. 6 the whole signal level changed after DBF and the suppression does not equal the normalized amplitude of Fig. 7. However this can be explained by the combined gain of the antenna, which focuses also to the meadow.

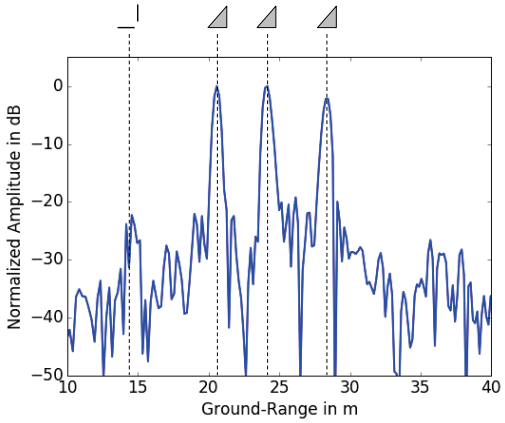

Figure 7: Range compressed data after DBF: $|u_{\mathrm{DBF}}(t)|^2$. Transmit and receive antenna beams looking to the same direction: $\Theta_\Delta = 0°$.

In antenna beam-configuration B, the transmit antenna points to the ground with a constant angular offset of $\Theta_\Delta = +6.8°$ with reference to the receive antenna beam (compare Fig. 5). Basically, the angular offset is obtained by adjusting the equivalent range distance from the antenna to a hypothetical target on ground using trigonometric functions. Looking to the result plotted in Fig. 8, the corner reflectors are suppressed, while the metal plates appear clearly as a single target. With respect to the single channel case, the resulting DBF gain measured at the maximum of the impulse response of the plates is 11.8 dB.

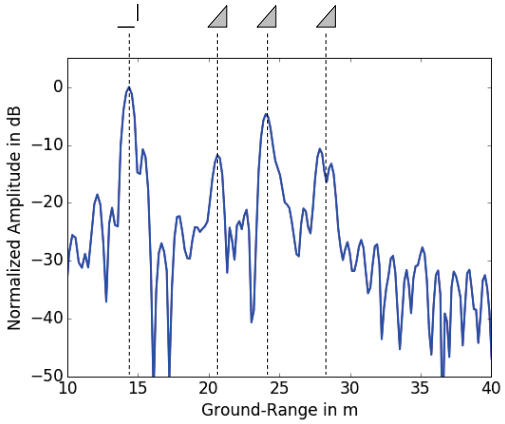

Figure 8: Range compressed data after DBF: $|u_{\mathrm{DBF}}(t)|^2$. Transmit and receive antenna beams looking to different directions with an offset of $\Theta_\Delta = 6.8°$.

A perfect suppression or focusing of the metal plates could not be achieved in both DBF modes, because of the geometrical extension of the metal plates along azimuth. In addition, the wide antenna beams in azimuth direction illuminate a significant part of the meadow with

non-negligible scattering coefficient, which also handicaps the aim of the experiment.

4 Conclusions

The concept of multipath propagation detection via MIMO techniques in single-pass tomography leads to an additional degree of freedom, which allows to extract additional information about the scattering behavior of the targets. Measurement results of a real radar scene have shown, that the suggested concept is working. For the future, it is recommended to repeat this preliminary measurement with simultaneously transmitted, orthogonal waveforms and extended volume scatterers in a real SAR mode. Since it is known, that the type of scattering mechanism has also an impact on the polarization state of the radar signal, a combination with fully polarimetric measurements would also be desired in a future experiment.

References

[1] Heimiller R. C., Belyea, J. E., and Tomlinson, P. G.: *Distributed array radar*, IEEE Transactions on Aerospace Electronic Systems, Vol. 19, pp. 831-839, 1983.

[2] Reigber, A. and Moreira, A.: *First demonstration of airborne SAR tomography using multibaseline L-band data*, IEEE Transactions on Geoscience and Remote Sensing, Vol. 38, No. 5, pp. 2142-2152, 2000.

[3] Krieger, G., Rommel, T., and Moreira, A.: *MIMO-SAR Tomography*, Proceedings EUSAR 2016.

[4] Rommel, T., Younis, M. and Krieger, G.: *An orthogonal waveform for fully polarimetric MIMO-SAR*, Proceedings in IEEE Radar Conference, pp. 887-891, 2014.

[5] Attia, E. and Steinberg, B. D.: *Self-cohering large antenna arrays using the spatial correlation properties of radar clutter*, IEEE Transactions on Antennas and Propagation, Vol. 37, pp. 30-38, 1989.